 MCB, vol.10, no.1, pp.43-65, 2013

Application of Numerical Methods to Elasticity Imaging

Benjamin Castaneda[*], Juvenal Ormachea[†], Paul Rodríguez[‡], and Kevin J.Parker[§]

Abstract: Elasticity imaging can be understood as the intersection of the study of biomechanical properties, imaging sciences, and physics. It was mainly motivated by the fact that pathological tissue presents an increased stiffness when compared to surrounding normal tissue. In the last two decades, research on elasticity imaging has been an international and interdisciplinary pursuit aiming to map the viscoelastic properties of tissue in order to provide clinically useful information. As a result, several modalities of elasticity imaging, mostly based on ultrasound but also on magnetic resonance imaging and optical coherence tomography, have been proposed and applied to a number of clinical applications: cancer diagnosis (prostate, breast, liver), hepatic cirrhosis, renal disease, thyroiditis, arterial plaque evaluation, wall stiffness in arteries, evaluation of thrombosis in veins, and many others. In this context, numerical methods are applied to solve forward and inverse problems implicit in the algorithms in order to estimate viscoelastic linear and nonlinear parameters, especially for quantitative elasticity imaging modalities. In this work, an introduction to elasticity imaging modalities is presented. The working principle of qualitative modalities (sonoelasticity, strain elastography, acoustic radiation force impulse) and quantitative modalities (Crawling Waves Sonoelastography, Spatially Modulated Ultrasound Radiation Force (SMURF), Supersonic Imaging) will be explained. Subsequently, the areas in which numerical methods can be applied to elasticity imaging are highlighted and discussed. Finally, we present a detailed example of applying total variation and AM-FM techniques to the estimation of elasticity.

Keywords: Elasticity imaging, inverse problems, FEM, total variation, shear velocity estimation, AM-FM.

[*] Laboratorio de Imágenes Médicas, Pontificia Universidad Católica del Perú
[†] Laboratorio de Imágenes Médicas, Pontificia Universidad Católica del Perú
[‡] Laboratorio de Procesamiento Digital de Señales, Pontificia Universidad Católica del Perú
[§] Electrical and Computer Engineering, University of Rochester

1 Introduction

Current medical imaging techniques generate representations of a physical parameter of the tissue being scanned. For example, ultrasound (US) represents the acoustic scattering and reflections within tissue, Magnetic Resonance Imaging (MRI) represents the proton density and relaxation times of the tissue, and X-ray imaging represents the attenuation of this type of radiation due to the tissue it traverses. Although these medical images are standardly used in current healthcare, there are still several medical applications to which they cannot be directly applied. For example, in the case of prostate or breast cancer, tumors could be invisible to US or MRI imaging [1].

Several studies have shown that changes in biomechanical properties of tissues are correlated to pathological changes [2]. In order to detect these changes, experts have performed manual palpation of the tissue for hundreds of years. This method can only be performed on lesions close to the surface of the human body. Small and deep tumors are typically missed [3].In this context, various techniques have been investigated and developed to estimate and image the elastic properties of tissue. The method in which stiffness of soft tissue is displayed as a parameter is termed elastography, or elasticity imaging [4]. The objective of elastography is to show the differences in tissue elasticity qualitatively and quantitatively. These techniques add new information which can be clinically useful to differentiate normal from abnormal tissue types [4].

These techniques have used different algorithms and applications of numerical methods to solve forward and inverse problems implicit in the algorithms to estimate different viscoelastic properties of soft tissues. Doyley et al [5] describe inversion schemes for each elastographic modality (quasi-static, harmonic and transient) and Barbone et al [6] focused their review on the mathematical structure and its computational solution for different biomechanical imaging.

In this article, we provide a review of current elasticity techniques (Section 2) and the application of numerical methods in this type of imaging (Section 3). In Section 4, we present the application of total variation and AM-FM algorithms to estimate locally the shear velocity of tissue in a particular type of elasticity imaging: Crawling Waves Sonoelastography.

2 Elastographic techniques

In the last 20 years, several groups have contributed to the field of elasticity imaging. While there are a variety of available techniques, they all share the following basic elements : (i) A mechanical force is applied to the tissue, (ii) the local motion provoked in the tissue is measured, and (iii) an elasticity parameter is estimated

from the measurements.

The different elastographic techniques can be classified by the type of information they provide (qualitative or quantitative), by the way the force is applied to the tissue (mechanical or acoustic radiation force), and by the modality used (US, MRI, or optical coherence tomography). In this paper, we only focus on ultrasound based elasticity imaging modalities. Table 1 shows a summary of these techniques.

Table 1: Summary of elasticity imaging modalities

Technique	**Qualitative or quantitative**	**Force applied**	**Parameter measured**	**Authors**	**First publication**	**Reference**
Sonoelastography	Qualitative	Mechanical	Vibration Amplitude	Lerner et al.	1987	[7]
Compression Elastography	Qualitative	Mechanical	Strain	Ophir et al.	1991	[8]
Shear Wave Elasticity Imaging	Quantitative	Radiation Force	Shear wave speed	Sarvazyan et al.	1998	[9]
Vibroacoustography	Quantitative	Radiation Force	Local acoustic response	Fatemi et al.	1999	[10]
Transient Elastography	Quantitative	Mechanical	Shear wave speed	Catheline et al.	1999	[11]
Acoustic Radiation Force Impulse	Qualitative	Radiation Force	Peak displacement	Nightingale et al.	1999	[12]
Crawling Wave Sonoelastography	Quantitative	Mechanical	Shear wave speed	Wu et al.	2004	[13]
Supersonic Shear Imaging	Quantitative	Radiation Force	Shear wave speed	Bercoff et al.	2004	[14]
SMURF	Quantitative	Radiation Force	Shear wave speed	McAleavey et al.	2007	[15]

2.1 Vibration amplitude sonoelastography

Lerner et al. proposed the idea of particle vibration displacement estimation using Doppler ultrasound [7]. Sonoelastography uses external mechanical sources to apply a low-frequency (20-1000 Hz) and low amplitude (20 to 100 μm) excitation to generate internal sinusoidal vibrations in the tissue under inspection. The low amplitude of excitation ensures a safe, non-invasive method and the low frequency

reduces the shear wave attenuation to enable deeper penetration in the tissue. The motion is then detected by Doppler ultrasound using a simple relationship between the Doppler spectral variance and the sinusoidal vibration amplitude of particles in the tissue.

Although, the main clinical focus of sonoelastography has been prostate cancer detection [16, 17, 18, 19], it has also been used in liver [16, 20], breast [21, 22] and kidney [16]. Vibration sonoelastography has shown better sensitivity and predictive values than B-mode imaging for *in vitro* results in prostate cancer [23].

The advantage of this technique is that it is compatible and easy to implement in commercially available US scanners. The main disadvantage is the need for an external vibration source which can introduce variability in the measurements. Figure 1 shows matching B-mode and sonoelastographic images of an *in vivo* human prostate. A cancerous tumor is shown in both images. The lack of vibration (represented by the void in the green background) in the sonoelastographic image is characteristic of a hard lesion adding to the diagnostic value of the B-mode image.

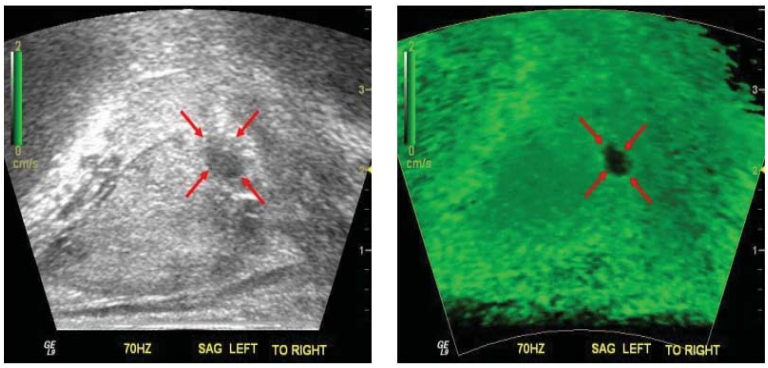

(a) (b)

Figure 1: (a) B-mode US and (b) sonoelastographic images from an *in vivo* prostate study. The sonoelastographic image reveals a stiff (cancerous) mass (denoted by arrows) in the middle of the image.

2.2 Compression elastography

This is arguably the most extensively used elastographic technique in clinical practice. In 1991, Ophir et al. [8] introduced an ultrasound technique for imaging soft tissue and strain profiles due to a compressive force applied to the medium. In this technique, radio-frequency (RF) signals from the same regions are compared before and after a small, quasistatic compression applied to the tissue. Displacement

between the two data sets is estimated using cross-correlation techniques. After that, the spatial derivative of the displacement is estimated to obtain a strain profile.

In this technique, the soft tissue can be understood as a simple union of 1-D springs. With this idea, the strain (ε) can be related to the internal stress (σ) using Hooke's law:

$$\sigma = E\varepsilon \tag{1}$$

Where E is the Young's modulus of the tissue. In order to simplify the estimation of the elasticity modulus, the internal stress distribution is typically assumed to be constant ($\sigma \approx 1$). Using this assumption, an approximate and relative estimation of Young's modulus is computed from the measured strain.

Compression elastography uses a transducer to produce the compression near the region of interest, which is very simple to implement in commercial US scanners. However, the quality of the image depends on the skill of the operator. There are also difficulties in compressing deeper organs and there is a tendency for objects to move out of plane during compression. Clinical applications include breast [24] and prostate [25] cancer detection, arterial plaque detection, treatment of lesions by High Intensity Focused US [26] and RF ablation in liver [27].

Figure 2 shows a compression (or strain) elastography image of a two layer phantom next to its matching B-mode image. The image shows that the upper part of the phantom is harder than the bottom. The image was taken with a Sonix Touch scanner (Ultrasonix, British Columbia, Canada) using a L14-5/38 probe at $10MHz$ in the Medical Image Research Laboratory at the Pontificia Universidad Católica del Perú.

2.3 Elasticity Imaging based on Acoustic Radiation Force

In addition to applying an external vibration or compression in the tissue, it is possible to create motion within tissue using acoustic radiation force (ARF). ARF is a phenomenon related to the attenuation of acoustic waves in a medium or tissue. Ultrasound waves transfer part of their momentum to the tissue and consequently push the local tissue from the inside and along the wave propagation direction [28].

In the case of soft tissue, absorption is the predominant attenuation mechanism in the medium. In this case, radiation force generated from an acoustic plane wave can be expressed as follows [12]:

$$F = \frac{2\alpha I}{c} \tag{2}$$

Where F is the acoustic radiation force, α is the absorption coefficient of the tissue,

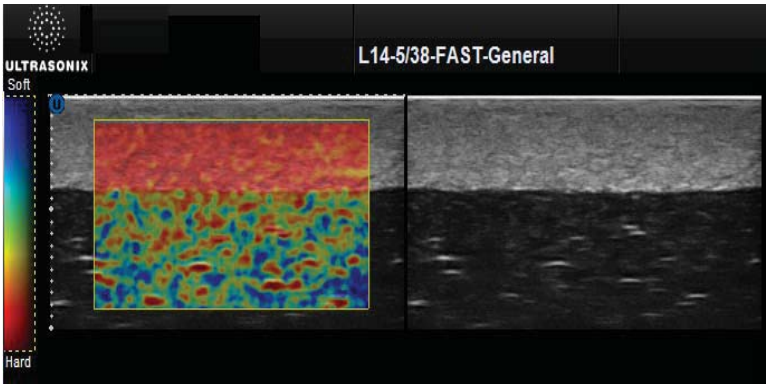

(a) (b)

Figure 2: (a) Compression (or strain) elastography image superimposed onto a B-mode image, and (b) B-mode image of a two layer gelatin phantom. The image shows that the upper part of the phantom is stiffer than the bottom.

I is the time-averaged acoustic beam intensity, and c is the speed of sound in the medium.

The spatial distribution of this radiation force is dependent on the focal configuration of the transducer, which is often characterized by the transducer f-number (F/#), and the spatial distribution absorption coefficient of the material.

As seen in Table 1, there are different elastography techniques which use ARF. In the case of quantitative techniques based in ARF, they estimate the shear wave speed (c_s) within the tissue. This parameter can be obtained by equation (3):

$$c_s = \sqrt{\frac{G}{\rho}} \tag{3}$$

Where G is the shear modulus and ρ is the density of the material.

In order to obtain a relationship between shear wave speed and the elasticity modulus, it is assumed that soft tissues are nearly incompressible, and, therefore, their Poisson's ratio (v) is approximately 0.5. The shear modulus can be related with the elasticity modulus by:

$$G = \frac{E}{2(1+v)} \approx \frac{E}{3} \tag{4}$$

Therefore, for a nearly incompressible biomaterial, a measurement of the shear

wave speed can be related with elasticity modulus as:

$$c_s \approx \sqrt{\frac{E}{3\rho}} \tag{5}$$

We can use (5) to obtain information about the stiffness of the material. For that reason, in elastographic imaging experiments (based on ARF or external forces), there has been increased attention on imaging shear wave properties.

Here, some of the elasticity techniques based on ARF are briefly explain:

2.3.1 Shear wave elasticity imaging

Shear wave elasticity imaging (SWEI) is used to image and characterize tissue structures using shear waves induced by ARF from a focused ultrasonic beam. Therefore, SWEI can use the same US transducer to generate the motion and the corresponding image.

In SWEI, the induced strain in the tissue can be highly localized because the induced shear waves are completely attenuated within a very limited region near the focal point of a focused ultrasound beam. In order to capture sufficient detail of the shear waves, frame rates of a few thousand images per second are needed. The shear wave propagation is tracked at different points adjacent to the focal point and the shear wave speed is obtained using cross-correlation algorithms. However, it is possible to increase the temperature of the tissue [9].

2.3.2 Acoustic Radiation Force Impulse (ARFI)

Nightingale et al. [12] proposed this technique. ARFI imaging uses a series of high intensity pushing beams of short duration (0.03-0.4 ms) to generate localized displacements (between 1 and 20 μm), and these displacements are tracked by ultrasound pulses of low pulse repetition frequencies (3 to 12 kHz) [29]. The response of the tissue to these forces is monitored to obtain images depicting the peak displacement or the time of recovery.

The same US transducer is used to generate the ARF and to track the resulting displacements. Thus, ARFI does not require additional hardware. However, as a disadvantage, the repetitive use of ARF increases the temperature of the tissue. For this reason, the intensity and the duration of the push pulses are limited to avoid heating and cavitation [29].

2.3.3 Supersonic Shear Imaging

Supersonic Shear Imaging (SSI) is an ultrasound-based technique that can visualize viscoelastic properties of soft tissue in real time [14]. It generates mechanical

vibration sources radiating at low-frequency using ultrasonic focused beams at different focal points in the axial direction. The resulting shear waves will interfere constructively along a cone shape, creating two intense plane shear waves (See Figure 3). These waves propagate through the medium and are affected by the tissue [14]. An ultrafast scanner ($>$ 5000 frames/s) is able to both generate this supersonic source and image the propagation of the resulting shear waves. The shear elasticity is mapped quantitatively from this propagation movie. SSI enables tissue elasticity estimation in less than 20 *ms*.

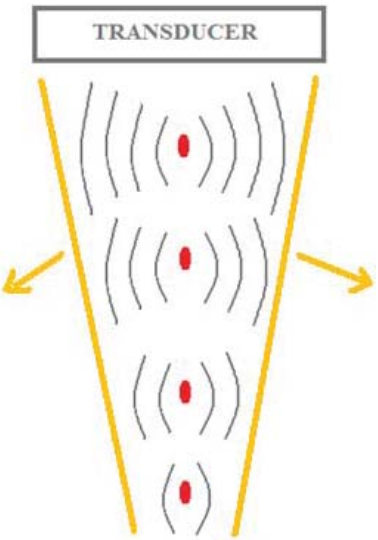

Figure 3: Radiation force pushes are induced by the transducer at different locations. As a result, shear waves are amplified in a cone shape (in orange), which increases the propagation distance of shear waves while acoustic power is minimized.

2.3.4 Spatially Modulated Ultrasound Radiation Force

In Spatially Modulated Ultrasound Radiation Force (SMURF), an acoustic radiation force with a well-defined intensity is used to generate shear waves with a known wavelength, λ, and then measures the frequency of the wave, f. [15]. The frequency of this wave, tracked along a single A-line, and λ are then used to estimate the shear modulus of the tissue. The advantage of this method is that it only requires a single location for measuring the displacement of the tissue and also gives quantitative information [30]. In Figure 4, a brief scheme of SMURF is presented. The shear speed can be estimated by forcing a known spatial frequency

and estimating the arrival time of the shear wave generated. Therefore, the shear modulus can be obtained from (6) and, subsequently, the elasticity modulus using equations (3) and (4).

$$c_s = f\lambda \tag{6}$$

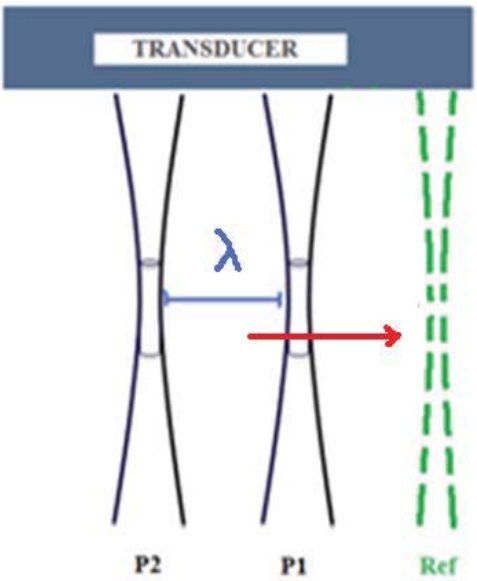

Figure 4: Brief scheme of SMURF. The red arrow indicates the direction of the generated shear wave. The tracking pulse is shown in green. SMURF generates shear waves of known source separation (λ). It measures the arrival time difference (ΔT) of the induced shear waves in an elastic medium.

Figure 5 presents the B-mode and the SMURF images obtained using a phantom. This phantom consisted of two layers, the upper layer stiffer than the bottom one.The color bar indicates the shear modulus of the material. The image was obtained using a Siemens Antares scanner in the McAleavey Laboratory at University of Rochester (Rochester, NY, USA).

ARF-based images have been applied to artery characterization [31, 32], colorectal tumor imaging [33], breast lesion detection [34], diagnosis of liver fibrosis [35], and guidance of RF ablation procedures for heart [36], liver [37], cornea stiffness [38], the elasticity time variation of the myocardium in the heart [39] and in tissue-mimicking phantoms [40].

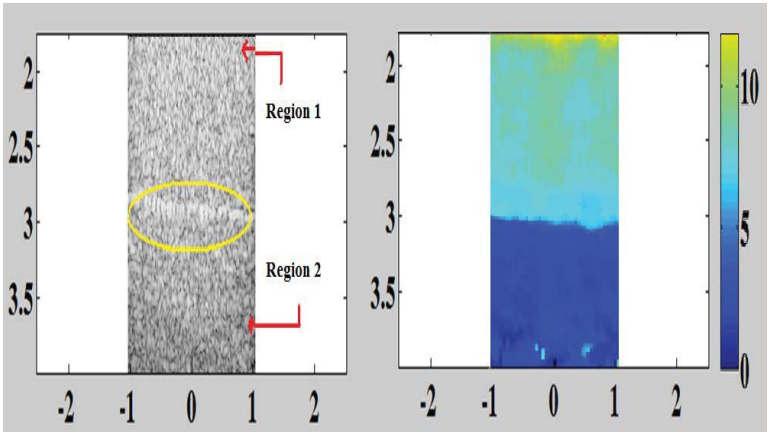

(a) (b)

Figure 5: (a) B-mode and (b) SMURF image of a gelatin phantom. The yellow circle indicates the boundary between region 1 and region 2 in the B-mode. We can see the elasticity contrast between the two regions in the SMURF image. The axial and lateral dimensions are in cm.

2.4 Transient Elastography

The concept of transient elastography was introduced in 1999 by Catheline et al. [11]. It is different from other elastographic techniques in that it uses an ultrafast ultrasound scanner to capture the propagation of shear waves generated by an external piston source. The rapid speed of transient elastography allows the separation of the transmitted wave from reflected waves. Thus, the technique is less sensitive to boundary conditions than other elastographic techniques. In addition, the acquisition time is short (less than 100 *ms*), which enables measurements on moving organs [11].

This technique has been applied to nonlinear elasticity measurements [41], liver fibrosis [11, 42], and breast tumor detection [43]. From this technology, the French company Echosens created the product Fibro scan which has become part of the standard of care for liver fibrosis [44].

2.5 Crawling Waves Sonoelastography

Crawling Wave Sonoelastography (CWS) is an elasticity imaging technique proposed by Wu et al. [13]. In this technique, two opposing shear wave vibration sources are operated at slightly offset frequencies and produce a slowly moving

interference pattern, termed Crawling Waves (CW), which is imaged in real time using vibration sonoelastography. The apparent velocity of CW is proportional to the underlying shear velocity of the tissue and can be used to estimate locally its elasticity modulus. This technique offers a quantitative estimation of the elastic properties of the tissue. In addition, the use of two vibration sources drives more mechanical energy into the tissue improving the Signal-to-Noise Ratio (SNR) [45].

The shear wave velocity can be estimated in different ways. Local frequency estimators were proposed by Wu et al. [13]. McLaughlin et al. [46] presented a method in which features of the CW and arrival times at points in the image plane are used to calculate the local shear velocity distribution in the image. Hoyt et al. [47] proposed a real-time estimator based on autocorrelation methods. In this technique, the shear wave velocity is estimated using (6). Here, f is the vibration frequency controlled and given by the vibration sources and λ is the shear wave wavelength measured from the image. In soft tissue, the relationship between Young's modulus (E) and shear wave velocity can be approximated using equation (5) and assuming that the material is incompressible.

Crawling wave sonoelastography has been successfully applied to detect radio frequency ablated hepatic lesions *in vitro* [48], to characterize human skeletal muscle *in vivo* [49, 50] and to characterize human prostate tissue *ex vivo* [45].

In Figure 6, we can see a crawling wave image of a gelatin phantom with a central stiffer inclusion. The interference pattern shows a different shear wave speed inside the red circle (a longer wavelength of the interference pattern) due to the stiffer material. This image was taken at the Sonoelasticity Laboratory of the University of Rochester using a GE Logiq 9 (GE Healthcare, Wauwatosa, WI, USA) scanner.

3 Numerical Methods in Elasticity Imaging

Numerical methods can be used to solve forward and inverse problems implicit in the algorithms to estimate the anisotropy, viscoelastic linear and non-linear parameters within soft tissues. Several groups have developed various elastographic approaches that examine first order approximation (methods based on stress uniformity [8] or local frequency estimation [7]), the direct problem elasticity imaging using Finite Elements Methods (FEM) and more complex models that cover the nonlinear viscoelasctic behavior [5]. Here we summarize how these methods have been applied to the different elastography modalities.

In compression elastography, the interpretation of the internal strain as a measure for the elasticity modulus (E) has several problems. First, the spatial derivative amplifies high frequency noise and, thus, the image quality is affected by the variance of the displacement estimation. Second, the assumption of a uniform stress distri-

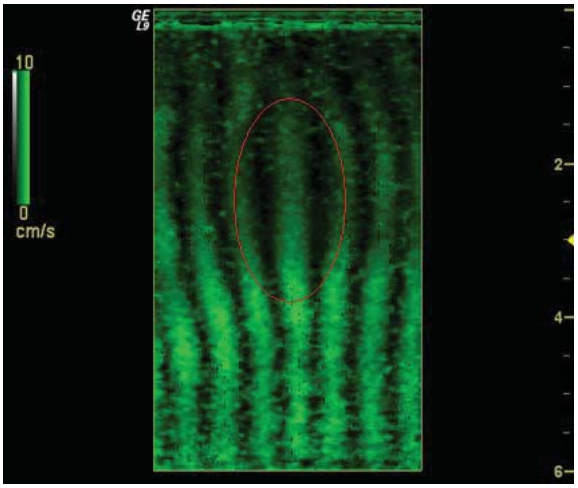

Figure 6: Crawling wave image of a gelatin phantom with a vibration frequency of 290Hz and0.35 Hz offset. The red circle shows an area of longer wavelength in the pattern and, therefore, of higher shear velocity.

bution can lead to strain image artifacts and diagnostic misinterpretations. Third, the tissue strain is a qualitative measure that cannot be compared quantitatively [51].

To overcome these drawbacks, Kallel et al. [52] proposed the reconstruction of elastic properties using elasto-mechanic models. In this work, a regularized inverse problem was formulated for only the axial component of the 3-D displacement vectors as a nonlinear least squares problem. Several groups have extended the reconstruction approach to use two or three components of the displacement vectors and have also modified the solver for the nonlinear problem [53, 54]. The reason to work with volumetric data is because 3-D motion tracking will significantly reduce echo signal decorrelation induced by tissue motion and deformation in the elevational direction that cannot be accurately tracked in 2-D echo data. Initial results using tissue-mimicking phantom have demonstrated that full 3D tracking can provide significantly higher quality strain images compared to 2D acquisition data.

In [55], Hall et al. show a review on their current status and recent developments to image in vivo nonlinear strain and tissue mechanical properties. They show the benefits using optimization approaches and different strain estimators (least squares strain estimator, total variational differentiation (TVD) strain estimator and two-point forward finite difference method). They mention that both the least squares and the TVD strain estimator produce less noisy strain estimates, whereas the two-

point finite difference method amplify the noise in the displacement estimates. Applications of their progress are illustrate in breast disease diagnosis and tumor ablation monitoring.

Eder et al. [51] reformulated the inverse reconstruction problem as an optimization problem and proposed the trust region reflective Newton solver to achieve a fast convergence of the reconstruction process. They computed the gradient information using the adjoin method [56] and used regularization to reduce the influences of the variance of the displacement estimation. The static external compression in the tissue generates a displacement u. They found u as a solution of a boundary value problem modeling the elasticity modulus as a parametric function e. Solving the problem for u yields a mapping $e \rightarrow u$, which they termed the forward problem of the reconstruction. They chose to implement a FEM solver based on a uniform rectangular grid, approximating e by a piecewise constant function, represented by a vector E (elasticity-modulus).

Thus, the FEM solver implements a mapping $(E \rightarrow U = \Phi(E))$by solving a linear system of equations. For the estimation of internal tissue displacement using ultrasound echo signals, they chose the block-matching algorithm [57] which is applied to the envelopes of the pre- and post-compressed US echo signals. They estimated the elasticity modulus (E_M) by solving the inverse problem $U_M = \Phi(E_M)$ with the consideration that displacement estimates (U_M) always have a certain estimation variance. To find an optimal E-modulus (E_ρ) which maps $\Phi(E)$ close to U_M, regularization was applied:

$$E_\rho = \texttt{argmin}\{G(E); E\} \tag{7}$$

$$G(E) = ||W \cdot (\Phi(E) - U_M)||_2^2 + \rho R(E) \tag{8}$$

Where $R(E)$ is a regularization measure and $||\cdot||_2^2$ denotes the L_2-norm of a vector. The regularization parameter ρ and the weights W determine the relative importance given to data fidelity versus regularity. W is the inverse of the standard deviation (σ) of the displacement estimation errors for each estimate ($W = 1/\sigma$).

To measure its regularity, they use the total variation of a function. However, the regularization process compromises the spatial resolution and contrast of the reconstructed result.

Pavan et al. [58] used FEM to show that elastic properties and the nonlinear strain/stress behavior have influence in the changes of image contrast as the material deforms due to compression. They simulated stress/strain data using the Verndа-Westmann constitutive hyperelastic model [59]. This model proved to be a good alternative to fit phantom [60] and breast tissue [61] stress/strain data. The strain contrast between inclusion and background was analyzed for different amounts of

strain using materials with different stiffness and nonlinearity. The strain contrast behavior with applied compression was affected by the nonlinearity of the inclusions. The clinical relevance of this work was that nonlinear elasticity provided information which could be used to distinguish various tissues.

Erkamp et al.[62] could increase differentiation between different materials types, modeling its nonlinear elastic properties. They performed simulations and measurements in agar-gelatine phantoms and fitted the data using a 3-D second order polynomial model. Their results show the potential to both increase the Contrast-to-Noise Ratio (CNR) in elasticity imaging and provide a new independent mechanism for tissue diferentiation without any sacrifice in spatial resolution.

Numerical methods were also applied to elasticity modalities based on ARF. Palmeri et al [63] evaluated the effect of temperature increase under several pushing schemes in ARFI imaging. For that, they developed a FEM to simulate the heating associated with ARFI imaging. They assumed that the change in the speed of sound with respect to temperature is linear for temperature changes less than $6^{\circ}C$ [64]. The model was implemented using two steps:(i) the spatially distributed acoustic intensity field was computed and the associated heat source function was estimated using equation (9), and (ii) FEM was used to determine the thermal response of the tissue.

$$q_v = 2\alpha I \tag{9}$$

Where $q_v[J/cm^3]$ is the rate of heat production per unit volume, $\alpha[Np/cm]$ is the absorption coefficient for soft tissue and $I[W/cm^2]$ is the acoustic beam intensity.

This work found that the temperature increase is greater for less-absorbing tissues, and more-absorbing tissues distribute the thermal energy over greater volumes in the near field. They also found that ARFI images can suffer from artifacts due to sound speed changes in the transducer and the tissue.

Bouchard et al. [65] described and evaluated various beam sequencing schemes which were designed to reduce acquisition time and heating. These techniques reduced the total number of radiation force impulses needed to generate an image and minimize the time between impulses. Tissue and transducer face heating which resulted from these schemes were assessed through FEM modeling and thermocouple measurements. They could reduce frame acquisition time incorporating a new beam sequencing (multiplexed and multi-time techniques) and parallel-receive beam forming into ARFI imaging. Results indicated that heating issues can be mitigated by employing ARFI acquisition sequences that utilize the highest track-to-excitation ratio.

Recently, Dhanaliwala et al. [66] proposed a new 1.5-D ARF transducer to reduce echo decorrelation and improve ARF image signal-to-noise. Echo decorrelation

improvements are achieved using the 1.5-D design in [67], and dedicated elements for each of the pushing and tracking functions. The model was validated and evaluated using FEM in terms of SNR and CNR. When compared to a conventional 1-D array, simulations showed that the 1.5-D ARFI array provided significantly improved displacement estimation, SNR, and CNR.

In crawling wave sonoelastography, McLaughlin et al. [68] used numerical methods to calculate the speed of the moving interference pattern using the arrival times of these same patterns. A geometric optics expansion was used to obtain equations (10) and (11), which are called the Eikonal equations:

$$|\nabla\phi(x)| = \sqrt{\rho/\mu} = 1/C_s \tag{10}$$

$$|\nabla\phi(x)| = \sqrt{\rho/(\lambda+2\mu)} = 1/C_p \tag{11}$$

Where $\phi(x)$ is the phase of the ultrasound wave, ρ is the density material, λ, μ are the Lamé constants, C_s and C_p are the shear and compression wave speeds, respectively.The Eikonal equations are related to the moving interference pattern arrival times, to the moving interference pattern speed, and then to the shear wave speed. To find the arrival times, they employed a cross-correlation technique and an inverse Eikonal solver, called the Level Curve Method, to compute the speed of the interference pattern.

To estimate the interference pattern speed (V), they used the spatially varying component of the phase, which is $\varphi(x) = \omega_1\phi_1 + \omega_2\phi_2$ for crawling waves, so:

$$V = \frac{\omega_1 - \omega_2}{|\nabla\varphi(x)|} = \frac{\Delta\omega}{|\nabla\varphi(x)|} \tag{12}$$

The goal in [67] was to calculate $V\alpha|\nabla\varphi(x)|^{-1}$ avoiding the essentially unstable calculation of dividing by derivatives of noisy data. To do that, a robust second order method approximated the speed of the moving interference pattern using the elementary idea that speed is distance divided by time. Thus, the interference pattern speed, V, was calculated with the inverse level curve method for the Arrival Time algorithm. With this parameter they showed the image as a function of $\frac{2\omega_1 F}{\Delta\omega}$.

Hoyt et al. [69] proposed a viscoelastic approach based on sonoelastography imaging. A viscoelastic Voigt model was fitted using nonlinear least-squares techniques to determine the frequency-independent shear modulus and shear viscosity estimates using crawling wave sonoelastography. They validated their technique using simulations, phantom studies and human studies. The phantom studies revealed a 1% error in shear modulus in comparison to results from a mechanical testing system. Investigations in healthy human skeletal muscles revealed that voluntarily

contracted muscles exhibit increases in both shear modulus and shear viscosity estimates as compared to relaxed muscles. The authors also observed an increase in shear speed with frequency.

4 AM-FM techniques and Crawling Waves Sonoelastography applied to the estimation of elasticity

4.1 Current estimation of shear wave speed in CWS

Hoyt et al. [47] proposed a real-time estimator based on autocorrelation methods. One of the main advantages of this method is its computational simplicity compared with color flow processing available in commercial US scanners.

The shear velocity in both axes, axial (x) and lateral (y), are computed as:

$$\begin{aligned} c_x &= \left| \frac{2\pi(f_s+\Delta f_s)T_x}{\Delta\theta_x} \right| \\ c_y &= \left| \frac{2\pi(f_s+\Delta f_s)T_y}{\Delta\theta_y} \right| \end{aligned} \tag{13}$$

Where f_s is the vibration frequency, Δf_s is the offset in frequency between the two vibration sources, T_x and T_y are the spatial spacing in the axial and lateral axes respectively and $\Delta\theta_x$, $\Delta\theta_y$ are the variation of the analytic signal phase in the axial and lateral axes respectively.

In practice, boundary conditions or slight misplacements in the experimental setup change the direction of the CW. Therefore, both estimations can be combined to obtain a single and more accurate estimate of the shear velocity of the sample, which was named a 2-D shear velocity estimate:

$$c_{s_{2D}} = \frac{c_x}{\sqrt{\left(\frac{c_x}{c_y}\right)^2 + 1}} \tag{14}$$

The result is an image which represents the local shear velocity of the tissue which is termed shear velocity sonoelastogram.

This method was applied to estimate the viscoelastic properties in human prostates [69], *ex vivo* thermal ablated lesions in liver [48], and human skeletal muscles [49]. However, this method is affected by wave reflections and results from the estimation show a bias depending on the initial phase of the signal in the local kernel.

4.2 AM-FM demodulation

The AM-FM representation of images allows us to model non-stationary image content in terms of amplitude and phase functions. The elements presented in the

image can be represented using [70]:

$$I(\xi) = \sum_{n=1}^{L} a_n(\xi)\cos(\varphi_n(\xi)) \tag{15}$$

Where $I(\xi) : \mathbb{R}^2 \to \mathbb{R}$ is the analyzed image, $\xi = (\xi_1, \xi_2) \in \mathbb{R}^2$, $L \in \mathbb{N}$, $a_n : \mathbb{R}^2 \to [0, \infty)$ and $\varphi_n : \mathbb{R}^2 \to \mathbb{R}$.

Equation (15) suggests that the L AM-FM component images, $a_n(\gamma)\cos(\varphi_n(\gamma))$, model the essential image modulation structure, the amplitude functions $a_n(\gamma)$ can be understood as the intensity of the region in the image, and the FM components $\cos(\varphi_n(\gamma))$ capture fast-changing spatial variability in image intensity [70].

Given the image $I(\xi)$, the computation of the AM-FM components involves the estimation of the instantaneous amplitude function $a_n(\xi)$, the instantaneous phase function $\varphi_n(\xi)$ and the instantaneous frequency $\omega_n = \nabla\varphi_n(\xi)$.

Standard reconstructions of $I(\xi)$ included the AM-FM Dominant and Channelized Component Analysis (DCA and CCA, respectively). In both methods, a filter bank is applied to the Hilbert-tranformed image, and then, the AM-FM demodulation of each band-pass filtered image is performed. In AM-FM reconstructions based on the CCA, a reasonably small number of locally coherent components are used. Those based on DCA only use one component from the channel with the maximum amplitude estimate. Nevertheless, both types of reconstructions are known to produce noticeable visual artifacts [71].

In [70], Rodriguez et al. proposed a method based on a regularized optimization of the estimates from the CCA, which obtained a small number of locally coherent components and simultaneously enforced a piece-wise smooth constraint for the amplitude functions. This method showed higher quality reconstructions than standard CCA and DCA reconstructions.

4.3 Crawling waves and AM-FM demodulation

As previously explained, in CWS, two opposing sources create an interference pattern imaged with Sonoelastography.

Under the plane wave assumption and considering a homogenous sample, the shear waves introduced by the right and left vibration sources can be described as follows [45]:

$$W_{right} = e^{-\alpha(x+\frac{D}{2})} \cdot e^{-i(k_1(x+\frac{D}{2})-w_1 t)} \tag{16}$$

$$W_{left} = e^{-\alpha(\frac{D}{2}-x)} \cdot e^{-i(k_2(\frac{D}{2}-x)-w_2 t)} \tag{17}$$

Where α is related to the attenuation of the wave in the sample, D is the distance between the sources, k_1 and k_2 are the wave numbers and w_1 and w_2 are the frequencies of the vibration sources.

The resulting pattern is the superposition of the two waves. Sonoelastography will image the squared signal of the envelope:

$$|u(x,t)|^2 = 2e^{(-\alpha D)}[\cosh(2\alpha x) + \cos(2kx)] \tag{18}$$

The CWS image represented in (18) can be understood as a signal with amplitude and frequency modulation. Therefore, we propose to apply AM-FM demodulation to estimate the local spatial frequency of the signal, and consequently, the shear wave velocity. Based on [70], we perform a Total Variation denoising with a non-standard exponent which enforces a non-negativity constraint [72] since the noise in the image is neither salt-and-pepper nor Gaussian. Finally, we generate a reconstructed image via [72] to perform the spatial frequency estimation.

Figure 7 shows some preliminary results of this technique. Matching (a) B-mode, (b) histological, (c) crawling waves, and (d) shear velocity images of an ex vivo prostate acquired just after radical prostatectomy. The acquisition was performed with a specially modified Logiq 9 US scanner (GE Healthcare, Milwaukee, WI, USA) and two external mechanical sources (Model 2706, Brüel & Kjaer, Naerum, Denmark) vibrating at 120 Hz and 0.25 Hz offset. The shear velocity estimation shows a stiffer region to the left of the gland which coincides with the outlined cancer in the histological image. However, it is also apparent that there is a visual artifact to the right side of the prostate. Although promising, it is necessary to validate this technique with more cases of study.

5 Conclusion

This article aims to present an introduction to elasticity imaging and the application of numerical methods in this topic. The working principle and clinical applications of qualitative modalities (sonoelasticity, strain elastography, acoustic radiation force impulse) and quantitative modalities (Crawling Waves Sonoelastography, SWEI, SMURF, Supersonic Imaging) are described. In this context, numerical methods can be used to solve forward and inverse problems implicit in the algorithms to estimate viscoelastic linear and nonlinear parameters. In particular, the Finite Element Method stands out as one of the most widespread approaches to solve the partial differential equations involved. We conclude by proposing a new technique which combines total variation and AM-FM demodulation techniques to estimate the shear velocity from crawling wave sonoelastography images.

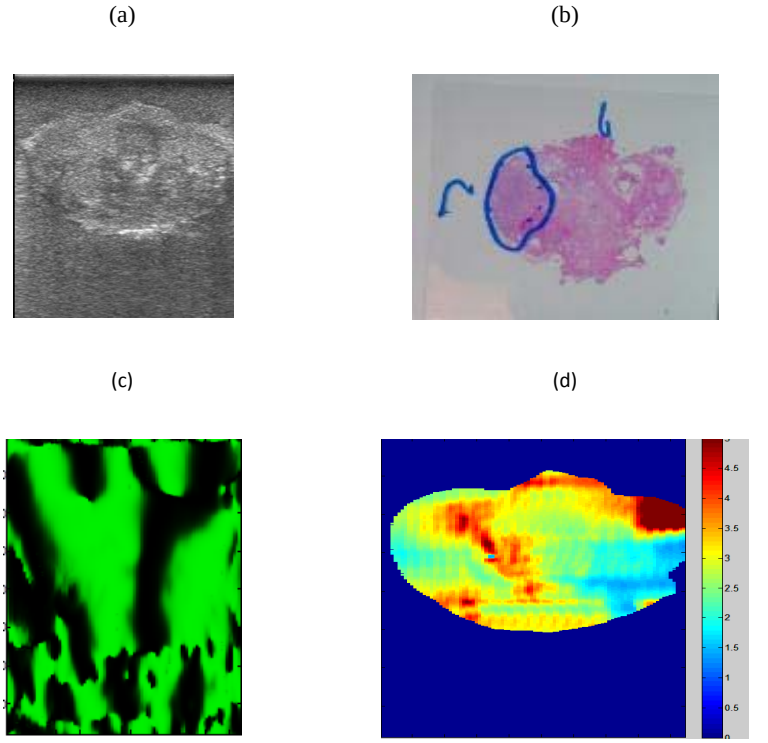

Figure 7: Matching (a) B-mode, (b) histology, (c) crawling waves, and(d) shear velocity images of an ex-vivo prostate

Reference

[1]Ophir, J., Alam, S. K., Garra, B., Kallel, F. & Konofagou, E. (1990) *Elastography: ultrasonic estimation and imaging of the elastic properties of tissues*. pp. 203–233.

[2]Parker, K. J., Taylor, L. S. & Gracewski, S. (2005) *Journal of the Acoustical Society of America* **117**, 2705–2712.

[3]Wu, Z. (2005) Ph.D. thesis (University of Rochester).

[4]Parker, K., Doyley, M. & Rubens, D. (2010) *Phys. Med. Biol.* **56**, R1–R29.

[5]Doyley, M. M. (2012) *Phys Med Biol.* **57**, 35–73.

[6]Barbone, P. E. & Oberai, A. A. (2010) *A review of the mathematical and computational foundations of biomechanical imaging* ed. De S, Mofrad MRK, Guilak F.

[7]Lerner, R. M. & Parker, K. J. (1987) *Sonoelasticity images derived from ultrasound signals in mechanically vibrated targets*.

[8]Ophir, J., Cespedes, I., Ponnekanti, H., Yazdi, Y. & Li, X. (1991) *Ultrason. Imaging.* **13**, 111–34.

[9]Sarvazyan, A. P., Rudenko, O. V., Swanson, S. D., Fowlkes, J. B. & Emelianov, S. Y. (1998) *Ultrasound Med Biol.* **24**, 1419–35.

[10]Fatemi, M. & Greenleaf, J. (1999) *Vibro-acoustography: An imaging modality based on ultrasound-stimulated acoustic emission*. Vol. 96, pp. 6603–08.

[11]Catheline, S., Wu, F. & Fink, M. (1999) *J. Acoust. Soc. Am.* **105**, 2941–50.

[12]Nightingale, K. R., Palmeri, M. L., Nightingale, R. W. & Trahey, G. E. (1999) *J. Proc. IEEE Ultrason. Symp.* pp. 1319–23.

[13]Wu, Z., Taylor, L. S., Rubens, D. J. & Parker, K. J. (2004) *Phys Med Biol.* **49**, 911–922.

[14]Bercoff, J., Tanter, M. & Fink, M. (2004) *IEEE Trans Ultrason Ferroelectr Freq Control* **51**, 396–409.

[15]McAleavey, S. A. & Menon, M. (2007) *Direct estimation of shear modulus using spatially modulated acoustic radiation force impulses*. pp. 558–6.

[16]Parker, K. J. & Lerner, R. M. (1992) *J. Ultrasound Med.* **11**, 387–92.

[17]Castaneda, B., Hoy, K., Westesson, K., An, L., Yao, J., Baxter, L., Joseph, J., Strang, J., Rubens, D. & Parker, K. (2009) *Performance of three-dimensional sonoelastography in prostate cancer detection: A comparison between ex vivo and in vivo experiments*. pp. 519–522.

[18]Taylor, L. S., Rubens, D. J., Porter, B. C., Wu, Z., Nigwekar, P. & Parker, K. J. (2005) *Radiology* **237**, 981–985.

[19]Hoyt, K., Parker, K. J. & Rubens, D. J. (2006) *Sonoelastographic Shear Velocity Imaging: Experiments on Tissue Phantom and Prostate*. pp. 1686–1689.

[20]Gheorghe, L., Iacob, S. & Gheorghe, C. (2008) *J Gastrointestin Liver Dis* **17**, 469–74.

[21]Yerli, H., Yilmaz, T., Kaskati, T. & Gulay, H. (2011) *J Ultrasound Med* **30**, 179–86.

[22]Scaperrotta, G., Ferranti, C., Costa, C., Mariani, L., Marchesini, M., Suman, L., Folini, C. & Bergonzi, S. (2008) *EurRadiol* **18**, 2381–9.

[23]Rubens, D. J., Hadley, M. A., Alam, S. K., Gao, L., Mayer, R. D. & Parker, K. J. (1995) *Radiology* **195**, 379–83.

[24]Garra, B. S., Cespedes, E. I., Ophir, J., Spratt, S. R., Zuurbier, R. A., Magnant, C. M. & Pennane, M. F. (1997) *Radiology* **202**, 79–86.

[25]Curiel, L., Souchon, R., Rouviere, O., Gelet, A. & Chapelon, J. Y. (2005) *Med. Biol.* **31**, 1461–8.

[26]Righetti, R., Kallel, F., Stafford, R. J., Price, R. E., Krouskop, T. A., Hazle, J. D. & Ophir, J. (1999) *Med. Biol.* **25**, 1099–113.

[27]Varghese, T., Techavipoo, U., Liu, W., Zagzebski, J. A., Chen, Q., Frank, G. & Lee, F. T. (2003) *Am. J. Roentgenol.* **181**, 701–7.

[28]Torr, G. (1984) *Am. J. Phys.* **52**, 402–08.

[29]Iyo, & Allison, Y. (2009) *Journal of Diagnostic Medical Sonography* **25**, 204–211.

[30]Mcaleavey, S., Collins, E., Kelly, J., Elegbe, E. & Menon, M. (2009) *Ultrasonic Imaging* **31**, 131–150.

[31]Trahey, G. E., Palmeri, M. L., Bentley, R. C. & Nightingale, K. (2009) *Ultrasound in Medicine & Biology* **30**, 1163–171.

[32]Couade, M., Pernot, M., Tanter, M., Prada, C., Messas, E. & Fink, M. (2008) *IEEE Ultrasonics Symposium* pp. 946–949.

[33]Palmeri, M., Frinkley, K., Zhai, L., Bentley, R., Ludwig, K., Gottfried, M. & Nightingale, K. (2004) *IEEE Ultrasonics Symposium* **1**, 744–47.

[34]Sharma, A. C., Soo, M. S., Trahey, G. E. & Nightingale, K. R. (2004) *IEEE Ultrasonics Symposium* **1**, 728–31.

[35]Fahey, B. J., Nelson, R. C., Bradway, D. P., Hsu, S. J., Dumont, D. M. & Trahey, G. E. (2008) *Phys Med Biol* **53**, 279–93.

[36]Hsu, S. J., Wolf, P. D., Fahey, B. J., Pinton, G. F., Dumont, D. M. & Trahey, G. E. (2005) *IEEE Ultrasonics Symposium* **2**, 1117–121.

[37]Fahey, B. J., Hsu, S. J., Wolf, P. D., Nelson, R. C. & Trahey, G. E. (2006) *Phys Med Biol* **51**, 3785–808.

[38]Tanter, M., Touboul, D., Gennisson, J. L., Bercoff, J. & Fink, M. (2009) *IEEE Transactions on Medical Imaging* **28**, 1881–1893.

[39]Couade, M., Pernot, M., Tanter, M., Messas, E., Bel, A., Ba, M., Hagege, A. & Fink, M. (2009) *IEEE International Ultrasonics Symposium* pp. 151–154.

[40]McAleavey, S., Collins, E., Kelly, J. & Elegbe, E. (2009) *Ultrasound Imaging* **31**, 131–150.

[41]Sandrin, L., Fourquet, B., Hasquenoph, J., Yon, S., Céline, F., Beaugrand, F. & Palau, R. (2003) *Ultrasound in Medicine & Biology* **29**, 1705–713.

[42]Moreno-Otero, R., Trapero-Marugan, M. & Mendoza, J. (2006) *GUT* **55**, 1055–056.

[43]Bercoff, J., Chaffai, S., Tanter, M., Sandrin, L., Catheline, S., Fink, M., Gennisson, J. L. & Meunier, M. (2003) *And Biology* **29**, 1387–1396.

[44]Foucher, J., Chanteloup, E., Vergniol, J., Castéra, L, LeBail, B., Adhoute, X., Bertet, J., Couzigou, P. & deLédinghen, V. (2006) *GUT* **55**, 403–8.

[45]Castaneda, B. (2009) Ph.D. thesis (University of Rochester).

[46]McLaughlin, J., Parker, K. J., Renzi, D. & Wu, Z. (2007) *J Acoust Soc Am* **121**, 2438–2446.

[47]Hoyt, K., Parker, K. J. & Rubens, D. J. (2007) *Ultrasound Med Biol* **33**, 1086–1097.

[48]Hoyt, K., Castaneda, B. & Parker, K. J. (2008) *Ultrasound Med. Biol.* **34**, 276–88.

[49]Hoyt, K., Castaneda, B. & Parker, K. J. (2007) *Muscle tissue characterization using quantitative sonoelastography: preliminary results*. pp. 365–8.

[50]Hoyt, K., Kneezel, T., Castaneda, B. & Parker, K. J. (2008) *Phys. Med. Biol.* **53**, 4063–80.

[51]Eder, A., Richter, M. & Kargel, C. (2012) *A new approach to improve the reconstruction quality in ultrasound elastography*. pp. 1908–1913.

[52]Kallel, F. & Bertrand, M. (1996) *IEEE Trans. Med. Imag.* **15**, 299–313.

[53]Li, J., Cui, Y., Kadour, M. & Noble, J. (2008) *IEEE Trans. Ultrason. Ferroelc. Freq. Contr.* **55**, 319–326.

[54]Richards, M., Barbone, P. & Oberai, A. (2009) *Phys. Med. Biol.* **54**, 757–779.

[55]Hall, T. J., Barbone, P., Oberai, A. A., Jiang, J., Dord, J. F., Goenezen, S. & Fisher, T. G. (2011) *Curr. Med. Imaging Rev.* **7**, 313–327.

[56]Oberai, A., Gokhale, N. & Feijoo, G. (2003) *Inverse Problems* **19**, 297–313.

[57]Hall, T., Zhu, Y., Spalding, C. & Cook, L. (2003) *Ultrasound Med. Biol.* **29**, 427–35.

[58]Pavan, T. Z. & Carneiro, A. O. (2011) *Change in strain image contrast with applied compression evaluated via finite elements analysis*.

[59]Veronda, D. R. & Westmann, R. A. (1970) *Journal of Biomechanics* **3**, 111–124.

[60]Pavan, T. Z., Madsen, E. L., Frank, G. R., Adilton, A., Carneiro, O. & Hall, T. J. (2010) *Physics in Medicine and Biology* **55**, 2679–2692.

[61]O'Hagan, [J. J. & Samani, A. (2009) *Physics in Medicine and Biology* **54**, 2557–2569.

[62]Erkamp, R. Q., Emelianov, S. Y., Skovoroda, A. R. & O'Donnell, M. (2004) *IEEE Trans UltrasonFerroelectr Freq. Control* **51**, 532–539.

[63]Palmeri, M. & Nightingale, K. (2004) *IEEE Trans. on Ultrason. Ferroelect. and Freq. Contr.* **51**, 551–565.

[64]Seip, R., Baren, P. Van, Cain, C. & Ebbini, E. (1996) *IEEE Trans. Ultrason., Ferroelect., Freq. Contr.* **43**, 1063–1073.

[65]Bouchard, R., Dahl, J., Hsu, S., Palmeri, M. & Trahey, G. (2009) *IEEE Trans. Ultrason., Ferroelect. Freq. Contr.* **56**, 63–76.

[66]Dhanaliwala, A. H., Hossack, J. & Mauldin, F. W. (2012) *IEEE Trans. Ultrason., Ferroelect. Freq. Contr.* **59**, 1602–1608.

[67]Mauldin, F. W., Wildes, D. G., Chiao, R. Y., Daft, C. M., Smith, L. S. & Thomenius, K. E. (1997) *IEEE Trans. Ultrason. Ferroelectr. Freq. Control* **44**, 1027–1037.

[68]McLaughlin, J., Renzi, D., Parker, K. & Wu, Z. (2007) *J Acoust Soc Am.* **121**, 2438–46.

[69]Hoyt, K., Kneezel, T., Castaneda, B. & Parker, K. J. (2008) *Phys. Med. Biol.* **53**, 4063–4080.

[70]Rodríguez, P., Murray, V. & Pattichis, M. S. (2010) *A Regularized Optimization Approach for AM-FM Reconstructions*. pp. 219–221.

[71]Murray, V., Rodríguez, P. & Pattichis, M. (2010) *IEEE TIP* **19**, 1138–1152.

[72]Rodríguez, P. (2010) *Multiplicative Updates Algorithm to Minimize the Generalized Total Variation Functional with a Non-negativity Constraint*. pp. 2509–2512.